(statistically indistinguishable from the trend of +3.6 (±2.5) Sv decade^{-1} reported last year). Similarly, the 35°S AMHT transport estimate has remained fairly constant for the last three years (mean northward values of 0.60 PW in 2014, 0.69 PW in 2015, and 0.63 PW in 2016). These estimates imply a virtually steady AMOC as well (the AMOC and AMHT being highly correlated). The AMHT trend at 35°S from July 2002 to August 2016 is +0.09 (±0.10) PW decade^{-1} (again statistically indistinguishable from the trend of +0.11 (±0.10) PW decade^{-1} reported last year). Variability at all latitudes in the Atlantic is not well correlated, and therefore, data from more than one latitude are needed to describe the state of the ocean. Interannual and higher frequencies dominate the variability in the MOC and MHT time series, and therefore long records will be needed to determine decadal and longer variability.

i. Global ocean phytoplankton—B. A. Franz, M. J. Behrenfeld, D. A. Siegel, and S. R. Signorini

Marine phytoplankton contribute roughly half the net primary production (NPP) on Earth, fixing atmospheric CO_2 into food that fuels global ocean ecosystems and drives biogeochemical cycles (e.g., Field et al. 1998; Falkowski et al. 1998). Satellite ocean color sensors, such as SeaWiFS (McClain 2009), MODIS (Esaias et al. 1998), and VIIRS (Oudrari et al. 2015), provide observations of sufficient frequency and geographic coverage to globally monitor changes in the near-surface concentrations of the phytoplankton pigment chlorophyll-a (Chl*a*; mg m^{-3}) that serve as a proxy for phytoplankton abundance. Here, global Chl*a* distributions for 2016 are evaluated within the context of the 19-year continuous record provided through the combined observations of SeaWiFS (1997–2010), MODIS on *Aqua* (MODISA, 2002–present), and VIIRS on Suomi-NPP (2011–present). All Chl*a* data used in this analysis correspond to version R2014.0 (https://oceancolor.gsfc.nasa.gov/reprocessing), which utilized common algorithms and calibration methods to maximize consistency in the multi-mission satellite record.

The spatial distribution of VIIRS annual mean Chl*a* for 2016 (Fig. 3.24) is consistent with the well-established, physically driven distribution of nutrients (Siegel et al. 2013) and surface mixed-layer light conditions (Behrenfeld et al. 2016). To assess changes in this distribution during 2016, mean values for VIIRS Chl*a* in each month of the year were subtracted from monthly climatological means for MODISA (2003–11). These monthly fields were then averaged to produce the global chlorophyll anomaly map for 2016

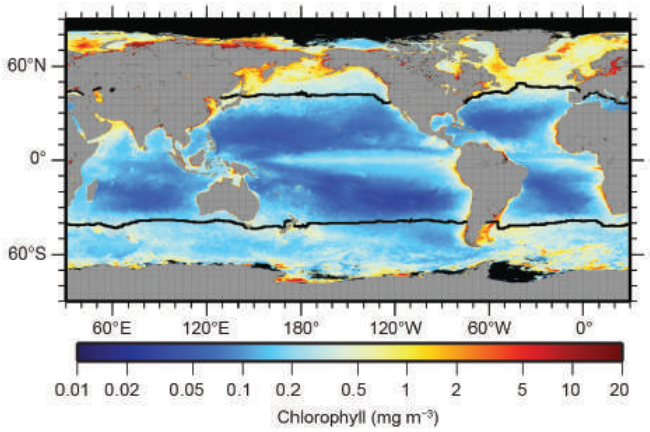

Fig. 3.24. Annual mean Chl*a* distribution (mg m^{-3}) derived from VIIRS for year 2016. Also shown is the location of the mean 15°C SST isotherm (black lines) delineating the boundary of the PSO. Chl*a* data are from NASA Reprocessing version 2014.0. Data are averaged into geo-referenced equal area bins of approximately 4.6 × 4.6 km^2 and mapped to an equirectangular projection centered at 150°W.

(Fig. 3.25a). Identical calculations were performed on MODISA sea surface temperature (SST; °C) data to produce an equivalent SST annual mean anomaly (Fig. 3.25b). The relationship between resultant annual anomalies in Chl*a* and SST are shown in Fig. 3.25c.

The dominant driver of phytoplankton Chl*a* change during 2016 was a climatic shift from El Niño to La Niña conditions. Accordingly, Chl*a* concentrations along the equatorial Pacific were elevated by 10%–20% over the climatological mean (red band in eastern equatorial Pacific in Fig. 3.25a). To the north and south of this band, Chl*a* concentrations were diminished relative to climatological values and inversely related with SST anomalies (dark blue areas above and below the equator in Fig. 3.25c). Within the boundaries of the permanently stratified ocean (PSO), delineated by the black lines in Figs. 3.24 and 3.25 at approximately 40°N and 40°S and defined as the region where annual average surface temperatures are >15°C (Behrenfeld et al. 2006), an inverse relationship was generally observed between Chl*a* and SST anomalies in the South Pacific (dark blue and dark red colors in Fig. 3.25c). By contrast, Pacific regions of the PSO north of the equator exhibited roughly an equal mix of positive and inverse relationships between Chl*a* and SST anomalies. Similarly, a mixture of Chl*a*–SST relationships was observed throughout the Atlantic and Indian sectors of the PSO. These findings for 2016 contrast with some previous findings (e.g., Behrenfeld et al. 2006, 2008, 2009; O'Malley et al. 2010; Siegel et al. 2012; Franz et al. 2013) and are further discussed below. In regions outside the PSO,

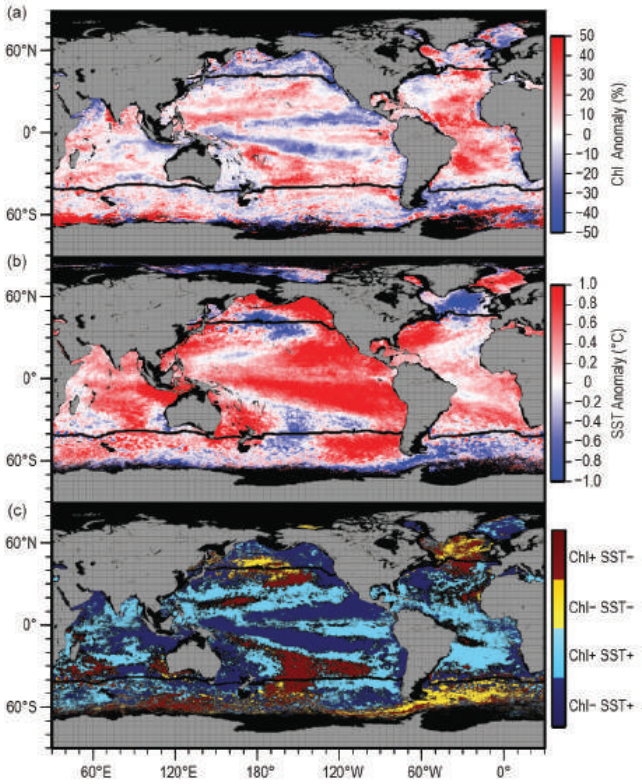

Fig. 3.25. Spatial distribution of averaged monthly 2016 (a) VIIRS Chl*a* anomalies and (b) MODISA SST anomalies, where monthly differences were derived relative to the MODISA 2003–11 climatological record. Chl*a* anomaly is expressed as % difference from climatology, while SST anomaly is shown as an absolute difference (°C). (c) identifies relationships between the sign of SST and Chl*a* anomalies from (a) and (b), with colors differentiating sign pairs and absolute changes of less than 3% in Chl*a* or 0.1°C in SST masked in black. Also shown is the location of the mean 15°C SST isotherm (black lines) delineating the PSO.

no clear relationship was observed between Chl*a* and SST anomalies (Fig. 3.25c), consistent with the previous studies cited above.

Over the 19-year time series of spatially integrated monthly mean Chl*a* values for the PSO (Fig. 3.26a), mean concentrations vary by ~20% (±0.03 mg m^{-3}) around a long-term average of ~0.15 mg m^{-3} (Fig. 3.26a). This variability includes significant seasonal cycles in Chl*a* distributions and responses to climatic events. The time series also demonstrates the high level of consistency between the overlapping periods of the SeaWiFS and MODISA missions and between the MODISA and VIIRS missions, thereby lending confidence in our extension of the long-term record using measurements from VIIRS alone.

Chl*a* monthly anomalies within the PSO (Fig. 3.26b) show variations of ±15% over the multimission time series. Notable for 2016, monthly anomalies in Chl*a* concentrations for the PSO trended consistently upward from an historical low at the start of the year (Franz et al. 2016), rising more than 20% to reach a 5% elevated state relative to the climatological reference by the end of the year. The link between these Chl*a* changes and a switch from El Niño to La Niña conditions is demonstrated as a corresponding decline in the multivariate ENSO index (MEI; Wolter and Timlin 1998; Fig. 3.26b, green diamonds, presented in the inverse to illustrate the covariation). Thus, 2016 was a transition year, which likely contributed to the weaker relationship between annual average Chl*a* and SST anomalies, as compared with similar analyses for previous years. However, monthly anomalies in PSO Chl*a* concentrations for 2016 remained consistent with the long-term ocean color record with respect to large-scale climate oscillations (Fig. 3.26b). This consistency is further evidenced in the spatial domain by comparing results shown in Fig. 3.25a with those reported by Franz et al. (2013), wherein a strikingly similar geographic distribution in Chl*a* anomalies was observed, but of opposite sign, for calendar year 2012 when the MEI was continuously trending upward.

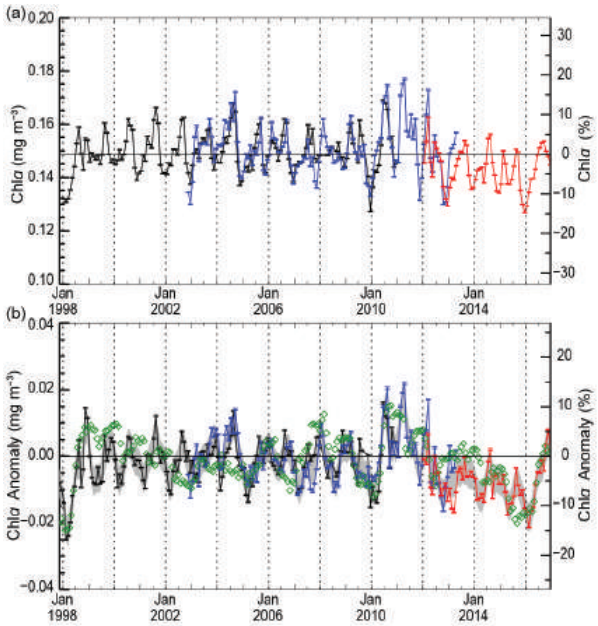

Fig. 3.26. 1998–2016, multimission record of Chl*a* averaged over the PSO for SeaWiFS (black), MODISA (blue), and VIIRS (red). (a) Independent record from each mission, with horizontal black line indicating the multimission mean Chl*a* concentration for the region (mg m^{-3}). (b) Monthly anomaly (%) for SeaWiFS, MODISA, and VIIRS after subtraction of the 9-year MODISA monthly climatological mean (2003–11). The gray region in (b) shows the averaged difference between SeaWiFS and MODISA over the common mission lifetime. Green diamonds show the MEI, inverted and scaled to match the range of the Chl*a* anomalies.

Surface layer Chl*a* concentrations, as derived from ocean color remote sensing, have long functioned as a central property for monitoring global changes in marine phytoplankton. Variability and trends in Chl*a* reflect both adjustments in phytoplankton biomass and physiology (or health). Both of these properties are mechanistically linked to physical properties of the upper ocean, as well as ecological relationships between phytoplankton and their zooplankton predators. Unraveling this diversity and often covariation of factors that influence Chl*a* concentrations is essential for correctly interpreting the implications of Chl*a* anomalies for ocean biogeochemistry and food webs. For example, inverse relationships between Chl*a* and SST can emerge from changes in either mixed-layer light levels or vertical nutrient flux, but these two mechanisms have opposite implications for phytoplankton NPP (Behrenfeld et al. 2016). An additional complication is that measured changes in ocean color often reflect, at least in part, changes in colored dissolved organic matter signals (Siegel et al. 2005) that are mistakenly attributed to Chl*a* changes (Siegel et al. 2013). Thus, while the satellite record of ocean color continues to provide critical insights on global processes, new insights and approaches are needed to fully understand the story these data are telling regarding relationships between climate and marine ecosystems.

j. Global ocean carbon cycle—R. A. Feely, R. Wanninkhof, P. Landschützer, B. R. Carter, and J. A. Triñanes

The global ocean is a major sink for anthropogenic carbon dioxide (CO_2) that is released into the atmosphere from fossil fuel combustion, cement production, and land use changes. Over the last decade the global ocean has continued to take up a substantial fraction of the anthropogenic carbon (C_{anth}) emissions and is therefore a major mediator of global climate change. Of the 10.2 (±0.7) Pg C yr^{-1} C_{anth} released during the period 2006–15, about 2.6 (±0.5) Pg C yr^{-1} (26%) accumulated in the ocean, 3.1 (±0.8) Pg C yr^{-1} (30%) accumulated on land, and 4.5 (±0.1) Pg C yr^{-1} (43%) remained in the atmosphere (Global Carbon Project 2016). This decadal ocean carbon uptake estimate is a consensus view based on a combination of measured decadal inventory changes, models, and global air–sea CO_2 flux estimates based on surface ocean partial pressure of CO_2 (pCO_2) measurements. Using ocean general circulation models that include biogeochemical parameterizations (OBGCMs) and inverse models that are validated with observations-based air–sea exchange fluxes and basin-scale ocean inventories, Le Quéré et al. (2016) have demonstrated that the oceanic anthropogenic carbon sink has grown from 1.2 (±0.5) Pg C yr^{-1} in the decade of the 1960s to 2.6 (±0.5) Pg C yr^{-1} in the decade from 2006 to 2015. Air–sea flux studies reported here indicate an ocean uptake of C_{anth} of 2.5 (±0.5) Pg C yr^{-1} for 2016, with the uncertainty being the standard deviation of monthly values.

1) Air–sea carbon dioxide fluxes

Ocean uptake of C_{anth} can be estimated from the net air–sea CO_2 flux derived from the bulk flux formula with air–sea differences in CO_2 partial pressure (ΔpCO_2) and gas transfer coefficients as input (Wanninkhof 2014). A steady contribution of carbon from continental runoff estimated at 0.45 Pg C yr^{-1} (Jacobson et al. 2007) is included to obtain the C_{anth}. The data source for pCO_2 are annual updates of surface water pCO_2 observations from the Surface Ocean CO_2 Atlas (SOCAT) composed of mooring and ship-based observations (Bakker et al. 2016). The ΔpCO_2 and a parameterization of the gas transfer with wind described in Wanninkhof (2014) are used to calculate the air–sea CO_2 fluxes. Increased observations and improved mapping techniques (e.g., Rödenbeck et al. 2015) now afford global pCO_2 fields at a 1° grid on monthly time scales with a lag of less than three months. This progress allows investigation of variability on subannual to decadal time scales.

The monthly 2016 ΔpCO_2 maps are based on an observation-based neural network approach (Landschützer et al. 2013, 2014) applied to biogeographical provinces. Surface temperature, sea surface salinity, climatological mixed-layer depth, satellite chlorophyll-a, and atmospheric CO_2 are used to establish relationships with surface ocean pCO_2 measurements and are applied where no observations exist. The 2016 air–sea estimate uses wind speeds from 2015 as consistent global wind products for 2016 have not been processed. Changes in winds over time have a small effect on gas transfer (Wanninkhof and Triñanes 2017) so this approximation should not have a determining impact on the interpretation of the air–sea CO_2 fluxes calculated for 2016.

The C_{anth} fluxes from 1982 to 2016 (Fig. 3.27) suggest a decreasing ocean sink in the first part of the record and a strong increase from 2001 onward. The amplitude of seasonal variability is ~1 Pg C with minimum uptake in June–September. The C_{anth} air–sea flux of 2.5 (±0.5) Pg C yr^{-1} in 2016 is 32% above the 2005–14 average of 1.9 (±0.5) Pg C yr^{-1}.

The average fluxes in 2016 (Fig. 3.28a) show the characteristic pattern of effluxes in the tropical regions, with the largest effluxes in the equatorial Pa-